ARTICLE   OPEN

Check for updates

Ultra-stable and tough bioinspired crack-based tactile sensor for small legged robots

Taewi Kim [1,5], Insic Hong [1,5], Minho Kim[1,5], Sunghoon Im [1,5], Yeonwook Roh [1], Changhwan Kim [1], Jongcheon Lim[2], Dongjin Kim[1], Jieun Park[1], Seunggon Lee[1], Daseul Lim[1], Junggwang Cho[1], Seokhaeng Huh[3], Seung-Un Jo[3], ChangHwan Kim[4], Je-Sung Koh [1✉], Seungyong Han [1✉] and Daeshik Kang [1✉]

For legged robots, collecting tactile information is essential for stable posture and efficient gait. However, mounting sensors on small robots weighing less than 1 kg remain challenges in terms of the sensor's durability, flexibility, sensitivity, and size. Crack-based sensors featuring ultra-sensitivity, small-size, and flexibility could be a promising candidate, but performance degradation due to crack growing by repeated use is a stumbling block. This paper presents an ultra-stable and tough bio-inspired crack-based sensor by controlling the crack depth using silver nanowire (Ag NW) mesh as a crack stop layer. The Ag NW mesh inspired by skin collagen structure effectively mitigated crack propagation. The sensor was very thin, lightweight, sensitive, and ultra-durable that maintains its sensitivity during 200,000 cycles of 0.5% strain. We demonstrate sensor's feasibility by implementing the tactile sensation to bio-inspired robots, and propose statistical and deep learning-based analysis methods which successfully distinguished terrain type.

npj Flexible Electronics (2023)7:22; https://doi.org/10.1038/s41528-023-00255-2

INTRODUCTION

Tactile sensors have been actively developed for robot's forceful interactions with environments such as grasping[1,2], tactile exploration[3,4], non-prehensile manipulation[5,6], in-hand manipulation[7,8], and human-robot interaction[9,10]. Off-road mobile robots also need to sense tactile information for obstacle avoidance, path planning, terrain recognition, and gait analysis. Especially for legged robots that running through discontinuous contact, the details of the interaction between their feet and ground can greatly affect the speed and efficiency of locomotion[11–13]. To remain maneuverable and agile in various terrains and environments, the robot must collect the current terrain information and control the legs' contact with the ground. The ground reaction force (GRF) is a crucial parameter that plays a significant role in the driving performance and automation of legged robots. By measuring the GRF, legged robots can adjust their movements to maintain balance and stability and adapt to different terrains. Moreover, the GRF data can be used to develop algorithms that enable legged robots to perform complex tasks and improve their overall efficiency[14]. These control demands are hardly achievable without the tactile sensing capabilities of each leg. However, tactile sensing in small (less than 1 kg) robots remains little used because there are challenges in sensor's durability, flexibility, sensitivity, and size. In this respect, the crack-based sensor can be a strong candidate for a small robot system.

Kang et al. developed an ultra-sensitive mechanosensor inspired by a spider's sensory organ[15–19]. They generated cracks on a metalized polymer to maximize resistance change by applied strain. The sensor was thin and sufficiently sensitive to strain, force, and vibrations to detect an arterial pulse, ant movements, and a voice. Currently, this spider-inspired sensor is the most sensitive among resistance-type sensors, with the added features

of high repeatability, high response speed, and low hysteresis[20]. Due to these advantages, it has been used in various applications such as motion monitoring[21,22], E-skin[23,24], robot control[25], acoustic sensor[26], and health monitoring[27,28] through crack engineering. However, the mechanosensor's sensitivity was unsteady when loads were repeatedly applied at high speed to the sensor, which led to accumulated stress in the crack tip, propagating crack growth[29].

Cracks cause stress concentration and significantly reduce material's fatigue life[30]. Therefore, so far, engineers and scientists have studied how to develop strong and tough (damage-tolerant) materials by resisting the generation and growth of cracks[31]. However, designing a crack-based sensor creates a situation in which cracks are easily generated on the surface and grow sufficiently deep, but should not grow beyond the designed depth. This is because the sensitivity of a crack-based sensor is proportional to the crack depth, but failure occurs if cracks get too deep. The mechanism by which cracks are formed in the deposited metal on the polymer substrate is very complex[32]. Depending on the material properties of the substrate and the deposited metal and the direction and magnitude of the applied stress, channel cracks or network cracks may occur, and their shape, size, depth, and length vary[33]. Advanced strategies and techniques are required to control the crack formation.

This study presents an ultra-stable, tough, and bio-inspired mechanical crack-based (ULTIMAC) strain sensor inspired by the tear resistance of skin collagen structure. The remarkable tear resistance of skin attributed to collagen fibril's stress redistribution was verified through previous experiments and fracture mechanics simulation[34,35]. The collagen structure is curvy and highly disordered in an unstressed state but becomes rearranged around the tensile load direction through various mechanisms[36].

[1]Multiscale Bio-inspired Technology Lab, Department of Mechanical Engineering, Ajou University, 206 World cup-ro, Yeongtong-gu, Suwon-si, Gyeonggi-do 16499, South Korea. [2]Weldon School of Biomedical Engineering, Purdue University, West Lafayette, IN, USA. [3]LIG Nex1, 333, Pangyo-ro, Bundang-gu, Seongnam-si, Gyeonggi-do 13488, Republic of Korea. [4]Defense Industry Technology Center, Agency for Defense Development, 61,Yeouidaebang-ro, Dongjak-gu, Seoul, Republic of Korea. [5]These authors contributed equally: Taewi Kim, Insic Hong, Minho Kim, Sunghoon Im. ✉email: jskoh@ajou.ac.kr; sy84han@ajou.ac.kr; dskang@ajou.ac.kr

npj

The rearranged structure also enhances toughness through bridging at the end of a tear, redistributing stress, and mitigating crack propagation[37].

We embedded a silver nanowire (Ag NW) mesh into the end of a designed crack depth as the crack stop layer to prevent crack propagation by mimicking the flexible collagen structure. The inserted mesh effectively prevented crack propagation and allowed the sensor to maintain high sensitivity at fast response times and low hysteresis. This paper outlines our sensor's performances such as sensitivity, repeatability, durability, hysteresis, and response time. We have assessed the sensor as having a sensitivity of GF 2000 at 0.5% strain, which remained almost unchanged even at a 0.5% strain during 200,000 cycles of repeated loads.

We also demonstrated that the ULTIMAC sensor was sufficiently thin, flexible, lightweight, compact, and extremely sensitive, but crucially, also highly durable, when integrated onto small legged robots. We implemented tactile sensing on the robot's foot by our sensor without making significant structural changes. By analyzing the data collected by the ULTIMAC sensor on a legged robot, we demonstrated that this sensor enable the robot to recognize the terrain and its current state.

RESULTS

Bio-inspired ULTIMAC sensor for small legged robots

The ULTIMAC sensor consisted of four layers: (1) a conducting and crack-initiating layer (Au and Cr), (2) a crack growing layer (Cured PI resin), (3) a crack stop layer (an Ag NW mesh), and (4) a supporting layer (PI film) (Fig. 1a). A scanning electron microscope (SEM) image of the sensor crack is shown in the upper right corner (Fig. 1a, inset). Our sensor's durability was dramatically improved by embedding a crack stop layer that was inspired by the skin's collagen structure.

The function of skin as the outermost organ of the body is to protect the muscles and internal organs from infections and injuries (Fig. 1b). Skin is composed of three layers: the epidermis, the dermis, and the hypodermis (Fig. 1c). The connective tissue layer between the dermis and the epidermis is comprised of dense and remarkably strong net-like collagen fibers (Fig. 1c, inset). These collagen fibers grant the skin astonishing resistance to tears as they distribute the concentrated stress at the end of tears.

Inspired by the remarkable tear resistance of skin, we have engineered a very thin (~10 μm), lightweight (~6 mg) and tough sensor using Ag NWs (Fig. 1d). We mimicked the collagen structure of skin to control the crack depth in our sensor and increase its durability (Fig. 1e). Ag NWs were easily woven into the mesh structure through spin coating, which gave the mesh a high aspect ratio (~3300) and high strength (~3 GPa) (Fig. 1e, inset).

As we outlined in the introduction, the miniature sensors for small robots must have very specific requirements: they must be small and lightweight, ultra-sensitive, and durable. We tested our sensor's feasibility of implementing motion and tactile sensation to a small legged robot by attaching our sensors to each leg of the robot (Fig. 1f). When equipped with our ULTIMAC sensor, ground interactions such as the magnitude and timing of GRF could be measured by the sensor as the robot moves over different types of terrain. Furthermore, by analyzing the peak heights (PH) and peak-to-peak intervals (PP) of the sensor signal, we could identify various information such as ground slope, terrain type, and ground vibration (Fig. 1g). Figure 1h shows the electrical response by the opening and closing of a metal crack when the ULTIMAC sensor is attached to the robot's. As the leg touches the ground, the resulting GRF deflects the compliant leg, widening the crack and consequently increasing the resistance of the sensor.

As highlighted in this paper, Fig. 1i shows a graphical illustration of crack initiation and propagation with strain cycles of conventional crack-based sensor and ULTIMAC sensor. The cracks initiated from the thin metal film, when it was subjected to critical strain, propagating into the polymer substrate[38]. The crack continues to propagate under repeated stress loads, resulting in deformation at the crack tip due to the accumulated stress, which affected the sensor's sensitivity. However, in the case of the ULTIMAC sensor with the Ag NW mesh embedded in the middle of the polymer substrate as a crack stop layer, the crack propagation was stopped after it reached the designated crack depth.
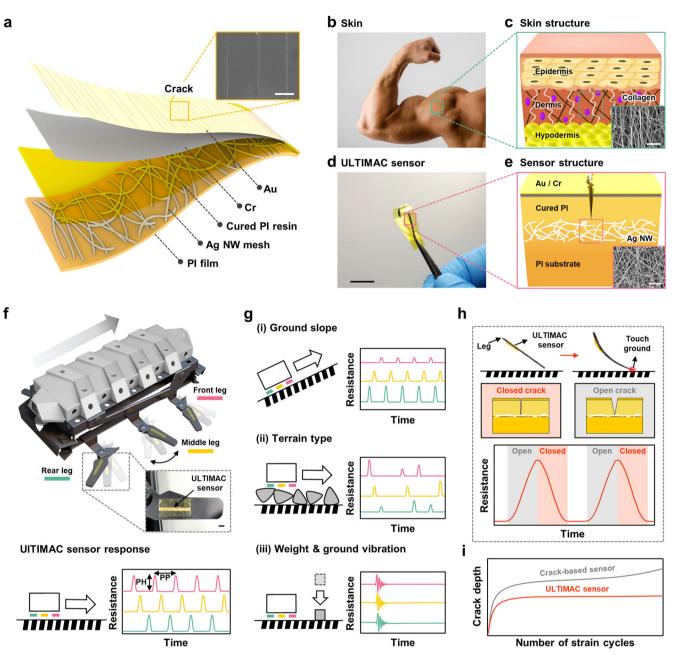
Fatigue behavior under crack propagation and characteristics of sensors with and without the crack stop layer

The nanowire mesh insertion allowed the sensor to maintain high sensitivity levels, but it was still necessary to test its durability. The crack-based sensor could have had low durability due to the stress and fatigue caused by crack propagation. Figure 2 analyzes how the sensor's durability was improved through the nanowire mesh insertion, which controlled the crack propagation.

Figure 2a shows the characteristic reaction to stress and fatigue in the event of crack propagation, under repeated mechanical loading and unloading, in the sensor. The numerical model of the crack-based sensor is simplified to an in-plane strain state because the cracks are channeled perpendicular to the direction of the mechanical load (Supplementary Fig. 1). Localized stress builds up at the end of the crack tip as the crack continues to propagate in-depth, under repeated loads[31,39]. As the crack reaches the elastic layer (the polymer substrate), it is either deflected along with the interface or penetrates the substrate[40–42]. Crack penetration leads to a rupture, delamination, and sensitivity degradation in the sensor[18,29,43]. Hence, the sensor is highly sensitive, but the substrate is weakened by crack propagation, ultimately leading to a fracture. Consequently, a crack-based sensor that is both highly sensitive and durable requires a control mechanism to grow a crack to the desired depth and then suppress that growth.

The sensors used in previous studies consisted of a supporting layer and a crack-propagating layer of polyethylene terephthalate (PET) film and polyurethane-acrylate (PUA) film[18,29,43]. Such sensors showed complex crack propagation behavior with mixed deflection and penetration due to the different mechanical properties between the two-layer materials (Supplementary Fig. 2)[44–46]. To prevent the partial delamination problem in PET and PUA materials' interface, we changed both materials to polyimide (PI). It was further possible to control the crack propagation depth by toughening the interface between the cured PI layer (as a crack-propagating layer) and the PI substrate (as a supporting layer) with the insertion of the crack stop layer (Ag NW). This additional layer redistributed the stress concentrated at the tip of the crack and bridged the crack interfaces[31,47–49]. The crack stop layer (Ag NW) had a toughening effect in the sensor that was tested through a finite-element method (FEM) that modeled crack interfacial deformations at a 2% strain. The FEM modeling result (Fig. 2b) shows that the crack-based sensor with and without an Ag NW layer. The sensor without the Ag NW layer accumulated stress at the tip of the crack, but the sensor with the inserted Ag NW layer effectively distributed the accumulated stress at the crack tip. As an additional case study, a sensor was fabricated and evaluated using a silver thin film as a crack stop layer, but undesirable micro scale cracks occurred in the silver thin film (Supplementary Fig. 3). In addition, when 2% strain was repeatedly applied, the initial resistance of the sensor continuously increased.
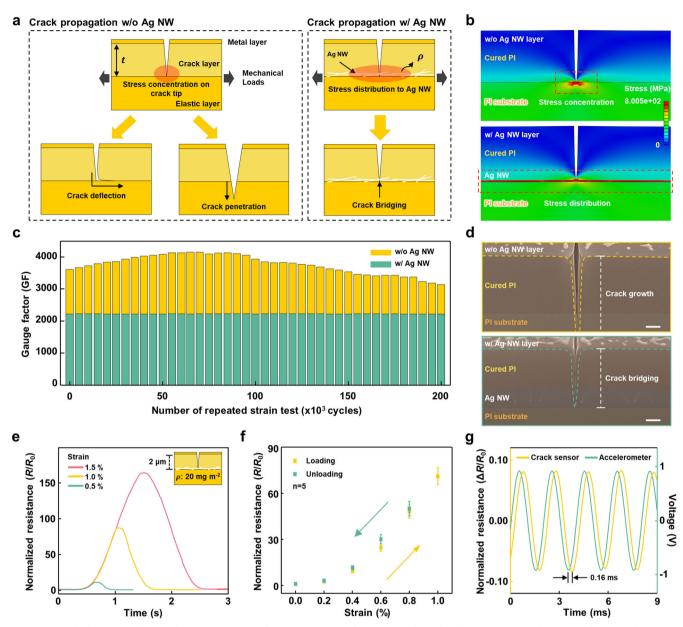
We conducted a fatigue test to evaluate the durability of the improved crack-based sensor with the Ag NW layer inserted. Figure 2c shows the variability of sensitivity in the crack-based sensors with and without the Ag NW layer during repeated cycles

Fig. 1 Overview of ULTIMAC sensor and its robotic application in terrain sensing. a Schematic layup of the ULTIMAC sensor used in this work. The inset shows the SEM image of nano metal cracks (Scale bar: 2 μm). **b** Image of skin that its remarkable toughness with high flexibility. **c** Skin consists of three layers: the epidermis, the dermis, and the hypodermis. The collagen fibers that make up most of the dermis are curvy and disordered in a non-stressed state but becomes rearranged toward tensile load direction under a stressed state. The inset shows the SEM image of artificial skin collagen (Scale bar: 10 μm). **d** Image of a tough ULTIMAC sensor. The lateral dimensions are 5 × 30 mm on 10 μm thick substrate. **e** The ULTIMC sensor consists of four layers: a metalized layer, a cured PI layer, an Ag NW mesh layer, and a PI substrate. The embedded Ag NW layer mitigates crack growth. The inset shows the SEM image of an Ag NW mesh (Scale bar: 1 μm). **f** Schematic illustration of a robotic application sensing terrain information by mounting an ULTIMAC sensors on robot feet, Inset: Photograph of an ULTIMAC sensor mounted on a robot foot (Scale bar: 1 mm). **g** Schematic illustration of terrain information derived from bending deformation data of robot feet. **h** The attached sensor to the compliant robot foot for detecting bending strain. **i** Schematic illustration of crack propagation with and without the Ag NW layer.

at a 0.5% strain. At the beginning of the test, the gauge factors (GF) determined by definition ($(\Delta R/R_0)/\varepsilon$) of the sensors was 2000 (with the Ag NW layer) and 3600 (without the Ag NW layer), respectively, where ΔR is the change in electrical resistance, R_0 is the initial electrical resistance. Without the Ag NW layer, the crack grows more in-depth, so the crack-based sensor without an Ag NW layer is more sensitive. The GF in the sensor without the Ag NW layer increased gradually from 3600 to 4000 over 100,000

cycles as the crack deepened, before decreasing to 3000 due to incomplete recovery from the stress accumulated at the crack tip[29,50]. In contrast, the crack-based sensor with the Ag NW layer had an almost constant GF (at 2000) and waveform from the start to the end of the test, implying that crack propagation was successfully mitigated in this sensor (Supplementary Fig. 4). When tested during 10,000,000 cycles at high speed (100 Hz) at a 0.1% strain, this sensor continued to maintain similar levels of sensitivity

Fig. 2 Fatigue behavior under crack propagation and characteristics of sensors with and without an Ag NW layer. a Schematic illustrations of possible crack propagation scenarios in a crack-based sensor in a plane strain state. **b** Finite-element method modeling of crack interface deformation with and without an Ag NW layer. **c** Durability test results (200,000 cycles at 0.5% strain) of the crack-based sensors with and without an Ag NW layer. **d** Cross-sectional SEM images of the crack-based sensors with and without an Ag NW layer (Scale bar: 500 nm). **e** Loading-unloading sensor behavior under various final strain conditions. **f** Loading-unloading behavior of five different samples to test sensor reproducibility and hysteresis. **g** Response time of the sensor's resistance to 1 G 500 Hz vibration.

(Supplementary Fig. 5). Figure 2d shows cross-sectional SEM images of the crack-based sensors with and without the Ag NW layer, after marathon tests of 200,000 cycles under a 0.5% strain. The above red-dotted box is a cross-sectional SEM image of the crack-based sensor without the Ag NW layer, positioned at the interface between the cured PI (crack-propagating) layer and PI substrate (supporting layer). The image shows that the crack has penetrated into the PI substrate in this sensor. In contrast, the image (below blue-dotted box) of the sensor with the Ag NW layer shows that the embedded Ag NW layer forms a bridge spanning the crack interfaces and allows the strain energy near the crack tip to be dissipated[48,51]. In addition, we confirmed that the crack stop method can be applied to other polymer/nanowire combination through further experiments on two cases. Firstly, we applied Ag NW as a crack stop layer to the structure (Metal thin film/PUA/PET).

The Ag NW network was inserted as an interface between the 10 μm thick PUA and the 50 μm thick PET layers. The marathon test (0.5% strain, 30,000 cycle) results demonstrated that the sensor with Ag NW maintained a constant gauge factor (GF), while the GF of the sensor without Ag NW decreased due to crack growth (Supplementary Fig. 6a, b). After the marathon test, SEM inspection of the sensor's cross-sections confirmed that the Ag NW layer effectively mitigated crack propagation (Supplementary Fig. 6c, d). Secondly, we used cost-effective copper nanowire (Cu NW) network as a crack stop layer as an alternative to Ag NW (Supplementary Fig. 7a). The sensor fabricated with Cu NW had an almost constant GF during the marathon test (1% strain, 1000 cycles), indicating that other nanomaterials with high mechanical strength and stretchability can mitigate crack propagation (Supplementary Fig. 7b).

Figure 2e–g show the sensor's resistance change under strain, reproducibility, hysteresis, and response time, which may be considered essential characteristics. Figure 2e shows cyclic variations in the sensor's resistance under different final strains. As the graph indicates, the sensor's normalized resistance (R/R_0) increases non-linearly with applied strain. The graph in Fig. 2f shows the resistance of five separate sensors that were loaded to a 1% strain and unloaded to a 0% strain, showing the sensor's high reproducibility and negligible hysteresis. To test the sensor's response time, we conducted an inertial vibration test (1 G 500 Hz). The results in Fig. 2g show that the sensor with the Ag NW layer responded to vibrations within 0.16 ms. Moreover, the sensor's high-frequency response characteristic was validated by applying displacement loading (0–0.1 μm) at various frequencies ranging from 100 to 400 Hz. As shown in Supplementary Fig. 8, the response of the sensor had some nonlinearity but no degradation in performance.

Mechanical and electrical characteristics of the ULTIMAC sensor

In order to study the effects of added Ag NW density and cured PI thickness (as the crack-growing layer) on the sensor's sensitivity, we conducted a number of parameter studies. These included testing the properties of Ag NW layers of two different areal densities (20 mg m^{-2} and 40 mg m^{-2}). Figure 3a presents the SEM images of the Ag NW percolation network, spin-coated into a flexible and continuous network, with these two different areal densities. As outlined in the previous section, this Ag NW layer was inserted as a crack stop layer. To observe how the Ag NW network density affected the overall mechanical stiffness of the crack-based sensor, we conducted a tensile test of the sensor equipped with the two different densities of the Ag NW layer.

Figure 3b shows the differences in tensile stress in response to higher levels of strain in the sensor when equipped with different Ag NW densities. Based on the tensile stress-strain curves, we obtained mechanical properties of the sensors such as Young's modulus, tensile strength, elongation at break, and toughness (as summarized in Supplementary Table 1). As the density of the Ag NW layer increased, its tensile strength also increased. The tensile strength of an unequipped sensor (without the Ag NW layer) was 228.2 MPa, compared with 264.1 MPa and 300.7 MPa tensile strength for a sensor with lower-density (20 mg m^{-2}) and higher-density (40 mg m^{-2}) of Ag NW layer. The elongation at the break in the sensors with the Ag NW layers (with areal densities of 20 mg m^{-2} and 40 mg m^{-2}) increased to 35.5% and 44.4%, as compared with 25.6% for the unequipped sensor, i.e.: without an Ag NW layer. Consequently, the toughness of the sensor with the Ag NW layer was significantly increased, with the sensor equipped with the higher-density Ag NW layer (40 mg m^{-2}) increasing in toughness to 100.6 MJ m^{-3}. We also measured the toughness (the area in the tensile stress-strain curve) of the sensors equipped with the different densities of the Ag NW layer, which indicates the energy of mechanical deformation per volume that can be absorbed before causing a fracture[31]. This toughness was up to 2.2 times higher than in the sensor without an Ag NW layer (45.5 MJ m^{-3}).

To evaluate the overall effect of the inserted Ag NW layer on the sensor's sensitivity, we measured the crack gap displacement directly related to the sensor's conductance via SEM, according to applied strain on the sensor and Ag NW density (Fig. 3c, d). Figure 3c shows the average crack gap displacements of ten different spots in five samples, measured in the 0–2% strain range. It shows that applied strain on the sensor and crack gap displacement have a positive linear relationship, as previously demonstrated in earlier studies[18,43]. In addition, the crack gap displacement decreased as the Ag NW density increased at the designated crack depth (Supplementary Fig. 9). This result implies that as the density of Ag
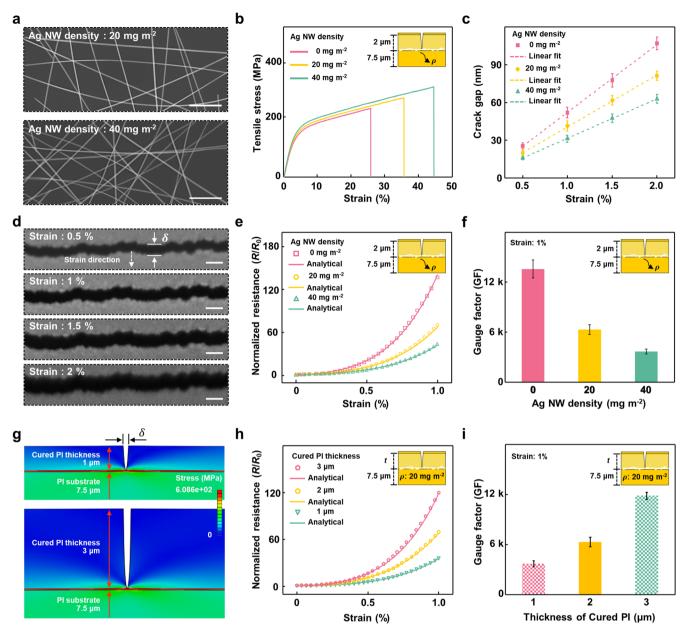
NW increases, the stress on crack tips decreases, reducing crack gap displacement. To support the above argument, we conducted a tensile test on Ag NW embedded polyimide film. The experiment result shows that Young's modulus of Ag NW embedded polyimide film significantly increases as the density of Ag NW increases (Supplementary Fig. 10).

Figure 3e shows variations of the resistance for strains of 0-1 %, depending on the areal density of the Ag NW layer. As previous studies have shown, sensor resistance increases with applied strain, following a quadratic function curve. As the graph illustrates, the sensor's resistance variances were well-matched with analytical values calculated by measuring the crack gap data. The equations used to calculation of resistance of ULTIMAC sensor are provided in Supplementary Note 1 and Supplementary Fig. 11. To summarize, as the areal density of the Ag NW layer increases, the sensor's GF at a 1% strain significantly decreases. The sensor's GF fell from 13,500 for the sensor without an Ag NW layer to 6300 for the sensor with the lower-density Ag NW layer (20 mg m^{-2}) to 3700 for the sensor with the higher-density Ag NW layer (40 mg m^{-2}) (Fig. 3f). These results indicate that increasing the density of the Ag NW layer improves the durability of the crack-based sensor by distributing the concentrated stress at the crack tip, but with the consequence of decreasing the sensor sensitivity by reducing the displacement of the crack gap.

One way to compensate for the decreased sensitivity in sensors with the Ag NW layer is through increasing the designated crack depth. We tested this approach through FEM simulation results of the crack gap displacement in the sensor, with varying thicknesses of the cured PI layer (Fig. 3g). In both cases, a 2% strain was applied to the sensor. The results show that the crack gap displacements were 76 nm and 113 nm when the cured PI layer had a thickness of 1 μm (top image) and 3 μm (bottom image). This result shows that the crack gap displacement, which is directly related to the sensitivity of the sensor, is significantly changed by adjusting the cured PI thickness. We also measured variations in sensor resistance with the lower-density Ag NW layer (20 mg m^{-2}) at a strain of 0–1% according to the change in the thickness of the cured PI layer (Fig. 3h). The results indicate that it is possible to tailor the sensor's sensitivity over a wide range of resistance (R/R_0) at a 1% strain: 38 to 120 by adjusting the designated crack depth. At a cured PI layer thickness of 2 μm, the sensor's GF at a 1% strain was 6300. When this cured PI layer was thinned (to 1 μm), the sensor's GF decreased to 3700, but when the cured PI layer was thickened (to 3 μm), the GF increased to 11,800 (Fig. 3i). The above series of sensor sensitivity-related parametric research show the potential of ULTIMAC sensor to be successfully applied to various robotic legs with different modulus by tailoring the Ag NW density and the cured PI thickness.

Terrain sensing of the ULTIMAC sensor

After testing the various properties of ULTIMAC, we conducted robotic trials by attaching sensors to a bio-inspired legged robot. We used the commercially available robot which comprised of a rigid body frame and six legs with flexural joints. Its specifications are 140 mm in length, 57 mm in width, 60 mm in height and 136 g in weight. The motion mechanism of the robot mimics oar movements, as the circular input trajectory of the motor is transferred to the ends of the oar-like feet, following a circular output trajectory (Supplementary Fig. 12). The robot implements differential driving by moving its left and right legs respectively with two motors. We attached one sensor to base of each foot of the robot (a total of six sensors per robot), and sensors transduced various forces acting on the feet into variances of resistance (Supplementary Video 1; Supplementary Fig. 13). The attached sensors allowed us to know the robot's gait, stride frequency, and terrain type by analyzing peak-to-peak intervals (PPI) and peak heights (PH) of the signals (Fig. 4a, b) generated each time the
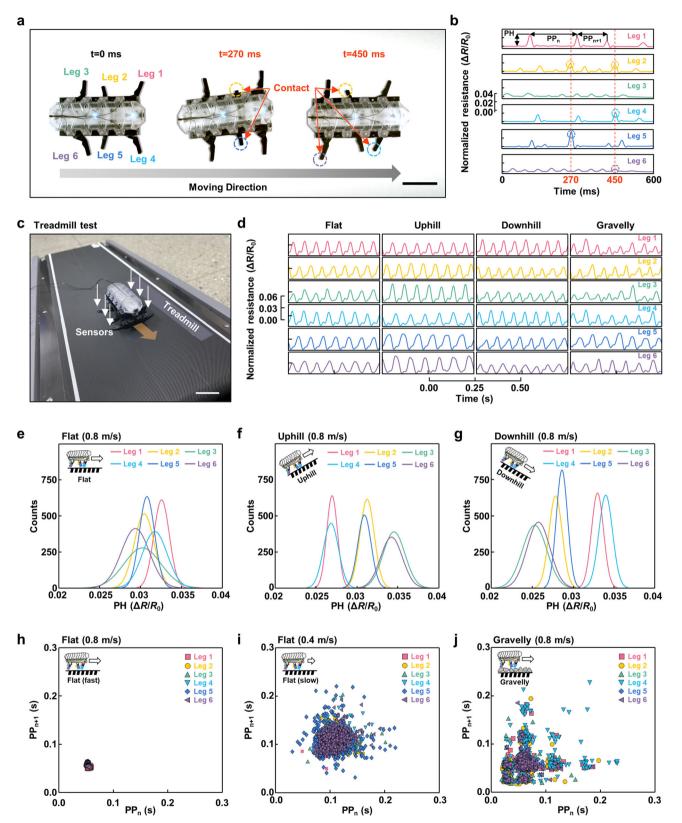
Fig. 3 Mechanical and electrical characteristics of the ULTIMAC sensor with the Ag NW layer. a SEM images of the percolated Ag NW network with different areal densities (20 mg m^{-2} and 40 mg m^{-2}) (Scale bar: 1 μm). **b** Uniaxial tensile tests of the ULTIMAC sensor, according to the two different densities of the Ag NW mesh. **c** Crack gap displacement (δ) change of crack-based sensor with Ag NW layer according to the applied strain and Ag NW density. **d** SEM images of crack-based sensor with Ag NW density (20 mg m^{-2}) according to the strain (Scale bar: 100 nm). **e** Normalized resistance changes in the ULTIMAC sensor, according to the two different Ag NW densities (ρ). **f** Gauge factor (GF) of the ULTIMAC sensor at 1% strain, according to Ag NW density. **g** Finite-element method modeling of the crack gap displacement, according to the thickness of the cured PI. **h** Normalized resistance changes of the ULTIMAC sensor, according to the thickness (t) of the cured PI. **i** GF of the ULTIMAC sensor at a 1% strain, according to the thickness of the cured PI.

robot's feet touched the ground (Supplementary Video 2). The sensor signals play a significant role in assessing the condition of both the robot and the ground. As illustrated in Supplementary Fig. 14 and Supplementary Video 3, the robot's movement across a gravel field resulted in yaw and pitch motions due to uneven contact between the robot's feet and the ground. Moreover, there were instances where the robot's legs did not touch the ground, producing distinctive features.

We conducted a long-term driving test on a treadmill to collect a large amount of sensor data (Fig. 4c). The robot ran on a total of four terrains: flat, uphill, downhill, and gravelly, and part of the collected sensor data is shown in Fig. 4d. The PH histograms of the sensors are obtained by plotting counts of the peak against PH. By

analyzing the PH histogram, we were able to determine the floor slope the robot was currently traveling on. When running on a flat ground, the load on the robot leg is evenly distributed so that the PH of each foot follows a Gaussian distribution (Fig. 4e). As the robot climbs a 30° incline, the robot's center of gravity shifts back, increasing the PH of the hind legs (legs 3 and 6) and decreasing the PH of the forelimbs (legs 1 and 4, Fig. 4f). In contrast, when the robot descends a 30° incline, the load on the forelimbs increases, resulting in a higher PH in the forelimbs and a lower PH in the hindlimbs (Fig. 4g).

We used the Poincaré plot to visualize the overall variability of the robot gait: a smaller, more focused plot represents higher gait stability, and a more scattered one indicates the irregularity of the

Fig. 4 Equipping the ULTIMAC on a bio-inspired legged robot: detection of terrain and analysis of gait. a Forward locomotion of the six-legged robot (Scale bar: 5 cm). **b** Sensor response of the robot running forward. **c** Long-term robot driving test setup using treadmill (Scale bar: 5 cm). **d** Normalized resistance changes of the sensor while robot running four terrains. (flat, uphill, downhill, gravelly). **e**–**g** Histograms of peak heights of the robot running flat, 30° uphill, and 30° downhill. **h** Poincaré plot of peak-to-peak interval of the robot running on a flat road at a speed of $0.8 \, \text{m s}^{-1}$. **i** Poincaré plot of peak-to-peak interval of the robot running on a flat road at a speed of $0.4 \, \text{m s}^{-1}$. **j** Poincaré plot of peak-to-peak interval of the robot running on a gravelly road at a speed of $0.8 \, \text{m s}^{-1}$.

gait. The Poincaré plot of PP is obtained by plotting PP_{n+1} against PP_n. We conducted the robot gait analysis on two types of floors: flat and gravelly road. When the robot ran on a flat road at maximum speed (0.8 m s^{-1}), the Poincaré plot formed a single dense cluster, indicating that the robot's gait was highly stable (Fig. 4h). However, when the speed of the robot is halved, the Poincaré plot also forms a cluster, but its density decreases, and a small number of values deviate from the mean (Fig. 4i). In the case of the gravelly road, the clusters appeared at several points with large variances as the contact made between the feet and the ground became irregular with increasing missed steps (Fig. 4j).

The ULTIMAC was also able to detect changes in the robot's center of gravity when an external load was applied. As shown in Supplementary Fig. 15, when a weight of 10 g is placed on the left central body of the robot, the resistance changes of the left sensor is larger than that of the right. Even small vibrations transmitted to the robot through the 5 mm thick woodrock board were detected by the sensor. When a 10 g weight was dropped from a height of 10 cm in front of the robot, the sensor was able to measure the vibration signals. In addition, the sensor showed high repeatability even for a total of 30,000 cycles measured while the robot ran at maximum speed (0.8 m s^{-1}) for 30 min at a stride frequency of 17 Hz (Supplementary Fig. 16 and Supplementary Video 4). Through the analysis of the strain exerted on the legs during running, it was determined that the sensor is applied a strain of about 0.3% during 1/3 cycle (34.65%), and the strain distribution was summarized as a histogram (Supplementary Fig. 17a). To estimate durability of ULTIMAC sensor under different strain amplitudes, a fatigue life model was used to fit the fatigue life of the sensor and compare it to that of commercial strain gauges (Supplementary Note 2 and Supplementary Fig. 17b).

Furthermore, not only feature-extracted data analysis, the data from ULTIMAC sensor also could be used as machine learning dataset. Since time-sequential characteristics of ULTIMAC sensor signal, we used one-dimensional convolutional neural network (1D-CNN) model as a classifier. We obtained 4 types of terrain (flat, uphill, downhill, gravelly) information through 6 sets of ULTIMAC sensor embedded in robot's legs (Fig. 4d). Then, we split the recorded data into training dataset and test dataset. 70% of recorded signal was used in training data, and rest of signal was used when evaluating the trained model. We sliced raw signal into 100 ms of fixed window (with 12.5 ms hopping) and labeled each segment according to terrain type (Fig. 5a). After slicing, (N, 128, 6) shape of input were fed into 1D-CNN model. Figure 5b shows data flow of training when 1st column of input is fed into the model. When sliced segment of ULTIMAC sensor signal is given, terrain-prediction probabilities are calculated as output. In training, only about 50 epochs were enough to predict the type of terrain in high accuracy (Fig. 5c). As the number of epochs increases, loss of train and validation set steeply decreases, and at the same time, prediction accuracy of train and validation set increases. Typical classification evaluation metrics such as ROC-AUC score was almost 1.0 (>0.99, Supplementary Fig. 18), and F1-score was also over 0.99 (Supplementary Fig. 19). In addition, confusion matrix of the trained model shows a good quality of prediction for terrain type from separated test dataset (Fig. 5d). The lowest accuracy of the prediction was 97.1%, in the gravelly floor. With same results, high accuracy of terrain prediction is depicted in polar coordinates (Fig. 5e). Two seconds of raw signal was extracted from the results. In figure, label 1 refer to flat, 2 to uphill, 3 to downhill and 4 to gravelly terrain. Otherwise, not only the terrain type, velocity of running robots can be predicted with high accuracy (>0.99, Supplementary Fig. 20). The results confirm that the robot can recognize changing terrain type in real-time during driving and prove the feasibility of autonomous control in future.
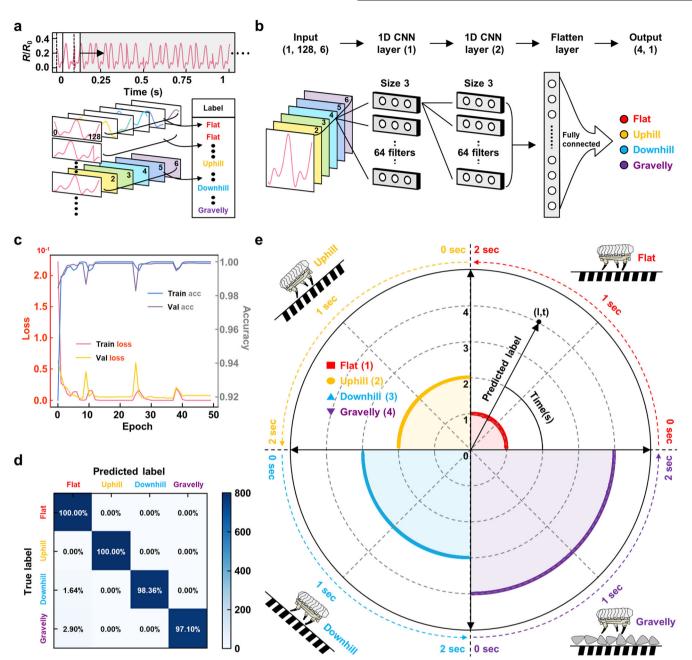
DISCUSSION

In summary, we developed a thin, flexible, lightweight, fast to respond, extremely sensitive, and even highly durable sensor through a nano-crack depth control method. We embedded an Ag NW mesh as a crack stop-layer to mitigate crack propagation at a designated crack depth. The mesh structure was inspired by the collagen fiber mesh in human skin, which has remarkable tear resistance and flexibility. This embedded Ag NW mesh layer successfully controlled crack propagation and maintained the sensor's overall sensitivity during our tests, even in strain trials over 200,000 cycles at a 0.5% strain. We determined the structural deformation between Ag NW's density or embedded depth and crack gap displacement through experiments and FEM simulation, which successfully improved sensor's fatigue life without adversely impacting the sensor's sensitivity. Integrating ULTIMAC strain sensors onto a small legged robot could serve various functions to provide critical information for feedback control. The integrated sensors could detect the generated force on each of the robot's strides, through mechanical signals transmitted to the robot feet while it was running. The sensor was also able to detect changes in the terrain type, road inclines, static loads applied to the robot, and even the floor's vibrations.

Our nano-crack depth control technology shows that the AgNWs which were mainly used to make flexible conductors, are also useful to develop an functional composite material capable of controlling crack propagation. This skin-inspired structure can be reconstructed with a combination of various materials considering the characteristics of the sensor to achieve, such as a combination of carbon fiber and elastomer to increase the flexibility and elasticity of the sensor. This technology can be applied to various fields using cracks, such as nanochannels, ion exchange channels, gas sensors, and nano-patterning. In particular, it can be applied to implement tactile and proprioceptive senses in small legged robots, which have limited weight and size. The statistical analysis method using PH and PP shown in this study visualizes the interaction between the leg moving at high speed and the ground so that it evaluates the driving stability of the robot. In addition, the ULTIMAC sensor connects robots to AI which is exploding the possibilities of robots recently. Terrain recognition by deep learning algorithms that can be applied to autonomous driving that adapts to terrain changes is just one example. In future research, the ULTIMAC sensor can implement adaptive control for optimizing energy efficiency or improving running speed of legged robots for each terrain. Furthermore, like a basilisk lizard freely running terrestrial-to-aquatic, it will be possible to implement a robot that can travel not only on solid terrain but also on water surface by precisely controlling each footstep.

METHODS

Ag NW synthesis

For a typical procedure of ultra-thin and long Ag NWs, 0.553 g poly-vinylpyrrolidone (PVP) (#437190, Sigma Aldrich, Co) and 0.00362 g Sodium chloride (NaCl) (#S7653, Sigma Aldrich, Co) are immersed into 70 ml glycerol (GL) (#324558, Sigma Aldrich, Co)[52,53]. The solution is stirred using a magnetic stir bar at 750 rpm and 80 °C. 0.50961 g silver nitrate (AgNO$_3$) (#10220, Sigma Aldrich, Co) put into 10 ml GL and dissolved it. Then, the solution of AgNO$_3$ is dumped into the mixture of PVP and continuously stirred until it is fully mixed. The well-dispersed mixture is transferred into a Teflon-lined autoclave and sealed for 7 h at 140 °C. The reactor is then cooled down to room temperature. The final product is centrifuged at 5000 rpm for 8 min. The purification process is proceeded at least 3 times to remove the PVP residue and impurities. The purified Ag NWs are stored in ethanol at room temperature. The resultant Ag NWs have a

Fig. 5 Terrain type classification by machine learning. a Pre-processing of raw ULTMAC sensor data. The data was sliced and labelled into true label of each terrain. **b** Overveiw procedure of machine learning of 1D-CNN model when pre-processed data is fed into as input. As an output, the model classifies one of the terrain types. **c** Training result by the number of epochs. Loss value decreases while accuracy increases. **d** Confusion matrix from prediction of test dataset. Average accuracy is 98.86. **e** Terrain prediction of a trained model in polar coordinates. Time flows in un-clockwise. Length of radius refers to the predicted label. True label of 1 refers to flat, 2 to uphill, 3 to downhill, and 4 to gravelly terrain.

constant diameter in the range of 30 nm and length in the range of 100–200 μm.

Cu NW synthesis

Cu NWs with a diameter of 40 nm and a length of 100 μm were synthesized by a hydrothermal method, involving the use of high-temperature and high-pressure water as the reaction medium[54,55]. Octadecylamine (ODA; 0.5 g; #10020, Sigma-Aldrich) was added to deionized water (DI Water; 70 mL) and agitated at 90 °C and 800 rpm using a hot plate stirrer under room temperature conditions for 30 min. Then, Ascorbic Acid (35 mg; #LRAA9724, Sigma-Aldrich) and copper (II) chloride dihydrate (CuCl2·2H2O;

68 mg; #BCBX0395, Sigma-Aldrich) were added sequentially and agitated with a magnetic stirrer at 800 rpm for 1 h at room temperature to obtain a blue emulsion. The blue emulsion was transferred to a Teflon-lined autoclave and hydrothermal treatment was performed in an oven preheated to 120 °C for 20 h. After the nanowire growth was completed, the reactor was cooled down to room temperature. The product was centrifuged at 6000 rpm for 5 min to remove the supernatant (residual solvent and reagent), and the precipitate was dispersed again in 20 mL of deionized water. Then, n-hexane (20 mL) was added and vigorously mixed for 20 s using a vortexer. After vortexing, the precipitate was allowed to settle for 30 min, and the precipitated CuNWs in the n-hexane phase were collected using a 1 mL

pipette. The obtained CuNWs (with an aspect ratio of 2500:1) were stored in isopropyl alcohol (IPA).

Fabrication of the ULTIMAC sensor

Fabrication process of the ULTIMAC sensor is detailed in the Supplementary information. The ULTIMAC sensor is composed of 4 layers: elastic substrate, crack stop layer, crack-penetrating layer, and a metal layer. As an elastic substrate, 7.5 μm thick PI film (3022-5 Kapton thin film, Chemplex, Co) was used. The Ag NW solution is repeatedly spin-coated to create percolated Ag NW network with a desired areal density on the substrate. Every time the Ag NW solution was spin-coated, the solvent should be evaporated by heating on 100 °C hot plate for 5 min. As a crack-penetrating layer, PI resin (POLYZEN 150 P, PICOMAX, Co) was spin-coated and cured in the nitrogen atmosphere (heating at 100 °C, 30 min ->200 °C, 30 min). After the curing process, we tested the durability against delamination issue in sensor application by T-peeling test using various commercial adhesive tapes (Supplementary Fig. 21). As shown in the Figure, the substrate PI and the cured PI maintained stable adhesion during the test. Then, 50 nm chrome (Cr) and 20 nm gold (Au) layers, which are optimal thicknesses for high sensitivity referenced by previous study[56], were deposited using a thermal evaporator (DDHT-SB015, Dae Dong Hitech, Co) with a shadow mask. The fabricated ULTIMAC sensor was stretched by 2% for 100 cycles with a rate of 20 mm min^{-1} using a material tester (3342 UTM, Instron, Co) to generate cracks.

FEM simulation

To simulate the crack's gap and stress distribution within the sensor, we conducted 2D finite element analysis of the 2% strain experiment using a commercial finite element analysis package (ABAQUS). We sketched and analyzed one of the numerous cracks with an initial crack width of 5 nm. The detailed size and material properties of the layers that make up the sensor are as follows: PI film (5×7.5 μm, Young's modulus of 2.5 GPa and Poisson's ratio of 0.34), Ag NW-PI composite (5 μm $\times 60$ nm, Young's modulus of 7.8 GPa and Poisson's ratio of 0.38), and cured PI resin (5×2 μm, Young's modulus of 1.8 GPa and Poisson's ratio of 0.34). The Young's modulus of the Ag NW-PI composite is determined by the general rule of mixtures which can be represented by following Eq. (1)[57].

$$E_c = fE_f + (1-f)E_m \tag{1}$$

$$f = \frac{V_f}{V_f + V_m} \tag{2}$$

Where V_f is the volume of the fibers, V_m is the volume of the matrix, E_f is the material property of the fibers and E_m is the material property of the matrix. Considering the crack's gap, we determined the layer's width to be 5 μm, and the metal layer was ignored because it was several tens of nm. Each layer is fully tied because there is sufficient bonding force between each layer. The analysis was performed by changing the thickness of the crack layer which is cured PI resin (1, 2, and 3 μm) and the presence or absence of the Ag NW-PI composite layer. To apply 2% strain to the sensor, we simply fixed one end of the sensor and pulled the other by 2% of the total width.

Tactile sensation on legged robot

To evaluate our sensor's practical applicability and various sensing functions, we mounted ULTIMAC sensors on the legged robot (Kamigami Scarrax Robot, ARO Tech, Co). The weigh of legged robot is 136 g. We used cyanoacrylate strain gauge adhesive to ensure strong and conformal contact between the sensors and robots (CN adhesive, Tokyo Sokki Kenkyujo, Co). We used conductive epoxy to connect wires on the sensor and additionally covered the wiring part with the commercial epoxy adhesive to fix it reliably. To prevent errors due to low battery, we removed the existing rechargeable lithium batteries, and the constant power was supplied to the robots using a power supply. The legged robot's movements were captured by high-speed camera (Phantom VEO640S, Vision Research, Co). A commercial treadmill was used for continuous measuring of legged robot's marathon test.

Characterization

The surface of Ag NW network and crack gap displacements were analyzed using a FE-SEM (S-4800, Hitachi, Ltd). The cross-sectional images of crack-based sensors were obtained using a focused ion beam (FIB) system (NOVA 600 Nanolab, FEI, Co). The resistance change of crack-based sensors was measured by a digital multimeter with a sampling rate of 500 Hz. (SIRIUS-SYSTEM, DEWESoft Korea, Ltd). The uniaxial tensile tests were conducted using a material tester (3342 UTM, Instron, Co). The tensile test specimen size is 5 mm (width) $\times$ 20 mm (length) and tensile speed is 5 mm min^{-1}.

1D-CNN model structure

Our neural network is composed of two 1d-convolutional neural network layers followed by dropout, MaxPooling, flatten, and fully connected layers. For convolutional layers, filter size is 3 and the number of filters is 64. For both layers, ReLU activation is used, and dropout is applied to prevent overfitting. We used consecutive fully connected layers to evenly distribute training parameters. At last, final output is transformed to the shape of probability distribution by softmax function, and cross entropy is used as a loss function, with 'adam' optimizer.

DATA AVAILABILITY

All data are available within the article or available from the authors upon reasonable request.

CODE AVAILABILITY

Codes for machine learning model used in this study are available on GitHub (https://github.com/sunghoon-most/6legged_ML).

REFERENCES

1. Bekiroglu, Y., Laaksonen, J., Jorgensen, J. A., Kyrki, V. & Kragic, D. Assessing grasp stability based on learning and haptic data. *IEEE Trans. Rob.* **27**, 616–629 (2011).
2. Dang, H. & Allen, P. K. Stable grasping under pose uncertainty using tactile feedback. *Auton. Robot.* **36**, 309–330 (2014).
3. Lepora, N. F., Martinez-Hernandez, U. & Prescott, T. J. Active Bayesian Perception for Simultaneous Object Localization and Identification. *In Robotics: Science and Systems*. 1–8 (2013).
4. Sutanto, G. et al. In *2019 International Conference on Robotics and Automation (ICRA)*. 3622–3628 (IEEE).
5. Veiga, F., Peters, J. & Hermans, T. Grip stabilization of novel objects using slip prediction. *IEEE Trans. Haptic* **11**, 531–542 (2018).
6. Tian, S. et al. In *2019 International Conference on Robotics and Automation (ICRA)*. 818–824 (IEEE).
7. She, Y. et al. Cable manipulation with a tactile-reactive gripper. *Int. J. Robot. Res.* **40**, 1385–1401 (2021).
8. Van Hoof, H., Hermans, T., Neumann, G. & Peters, J. In *2015 IEEE-RAS 15th International Conference on Humanoid Robots (Humanoids)*. 121–127 (IEEE).
9. Erickson, Z., Clever, H. M., Turk, G., Liu, C. K. & Kemp, C. C. In *2018 IEEE international conference on robotics and automation (ICRA)*. 4437–4444 (IEEE).

10. Park, D., Erickson, Z., Bhattacharjee, T. & Kemp, C. C. In *2016 IEEE International Conference on Robotics and Automation (ICRA)*. 407–414 (IEEE).
11. Li, C., Umbanhowar, P. B., Komsuoglu, H., Koditschek, D. E. & Goldman, D. I. Sensitive dependence of the motion of a legged robot on granular media. *Proc. Natl Acad. Sci. USA* **106**, 3029–3034 (2009).
12. Wu, X. A., Huh, T. M., Sabin, A., Suresh, S. A. & Cutkosky, M. R. Tactile sensing and terrain-based gait control for small legged robots. *IEEE Trans. Rob.* **36**, 15–27 (2019).
13. Qian, F. et al. Walking and Running on Yielding and Fluidizing Ground. 345–353 (*RSS*, 2013) http://www.roboticsproceedings.org/rss08/p44.html.
14. Wu, X. A., Huh, T. M., Mukherjee, R. & Cutkosky, M. Integrated ground reaction force sensing and terrain classification for small legged robots. *IEEE Robot. Autom. Lett.* **1**, 1125–1132 (2016).
15. Fratzl, P. & Barth, F. G. Biomaterial systems for mechanosensing and actuation. *Nature* **462**, 442–448 (2009).
16. Hößl, B., Böhm, H. J., Rammerstorfer, F. G. & Barth, F. G. Finite element modeling of arachnid slit sensilla—I. The mechanical significance of different slit arrays. *J. Comp. Physiol. A* **193**, 445–459 (2007).
17. Hößl, B., Böhm, H. J., Schaber, C. F., Rammerstorfer, F. G. & Barth, F. G. Finite element modeling of arachnid slit sensilla: II. Actual lyriform organs and the face deformations of the individual slits. *J. Comp. Physiol. A* **195**, 881–894 (2009).
18. Kang, D. et al. Ultrasensitive mechanical crack-based sensor inspired by the spider sensory system. *Nature* **516**, 222–226 (2014).
19. Politi, Y., Bertinetti, L., Fratzl, P. & Barth, F. G. The spider cuticle: a remarkable material toolbox for functional diversity. *Philos. Trans. R. Soc. A* **379**, 20200332 (2021).
20. Choi, Y. W. et al. Ultra-sensitive pressure sensor based on guided straight mechanical cracks. *Sci. Rep.* **7**, 1–8 (2017).
21. Qu, X. et al. Crack-based core-sheath fiber strain sensors with an ultralow detection limit and an ultrawide working range. *ACS Appl. Mater. Interfaces* **14**, 29167–29175 (2022).
22. Zhou, Y. et al. Significant stretchability enhancement of a crack-based strain sensor combined with high sensitivity and superior durability for motion monitoring. *ACS Appl. Mater. Interfaces* **11**, 7405–7414 (2019).
23. Kim, K. K. et al. A deep-learned skin sensor decoding the epicentral human motions. *Nat. Commun.* **11**, 1–8 (2020).
24. Li, J. et al. Visually aided tactile enhancement system based on ultrathin highly sensitive crack-based strain sensors. *Appl. Phys. Rev.* **7**, 011404 (2020).
25. Wu, J. et al. Sheath–core fiber strain sensors driven by in-situ crack and elastic effects in graphite nanoplate composites. *ACS Appl. Nano Mater.* **2**, 750–759 (2019).
26. Gong, S. et al. A soft resistive acoustic sensor based on suspended standing nanowire membranes with point crack design. *Adv. Funct. Mater.* **30**, 1910717 (2020).
27. Park, B. et al. Strain-visualization with ultrasensitive nanoscale crack-based sensor assembled with hierarchical thermochromic membrane. *Adv. Funct. Mater.* **29**, 1903360 (2019).
28. Roh, Y. et al. Vital signal sensing and manipulation of a microscale organ with a multifunctional soft gripper. *Sci. Robot.* **6**, eabi6774 (2021).
29. Park, B. et al. A semi-permanent and durable nanoscale-crack-based sensor by on-demand healing. *Nanoscale* **10**, 4354–4360 (2018).
30. Anderson, T. L. *Fracture mechanics: fundamentals and applications*. (CRC press), (2017).
31. Ritchie, R. O. The conflicts between strength and toughness. *Nat. Mater.* **10**, 817–822 (2011).
32. Thouless, M. Crack spacing in brittle films on elastic substrates. *J. Am. Ceram. Soc.* **73**, 2144–2146 (1990).
33. Zhang, C., Sun, J., Lu, Y. & Liu, J. Nanocrack-based strain sensors. *J. Mater. Chem. C.* **9**, 754–772 (2021).
34. Bircher, K., Zündel, M., Pensalfini, M., Ehret, A. E. & Mazza, E. Tear resistance of soft collagenous tissues. *Nat. Commun.* **10**, 792 (2019).
35. Wegst, U. & Ashby, M. The mechanical efficiency of natural materials. *Philos. Mag.* **84**, 2167–2186 (2004).
36. Yang, W. et al. On the tear resistance of skin. *Nat. Commun.* **6**, 1–10 (2015).
37. Sherman, V. R., Yang, W. & Meyers, M. A. The materials science of collagen. *J. Mech. Behav. Biomed. Mater.* **52**, 22–50 (2015).
38. Thouless, M., Li, Z., Douville, N. & Takayama, S. Periodic cracking of films supported on compliant substrates. *J. Mech. Phys. Solids* **59**, 1927–1937 (2011).
39. Ritchie, R. Mechanisms of fatigue crack propagation in metals, ceramics and composites: role of crack tip shielding. *Mater. Sci. Eng. A* **103**, 15–28 (1988).
40. Barthelat, F. Architectured materials in engineering and biology: fabrication, structure, mechanics and performance. *Int. Mater. Rev.* **60**, 413–430 (2015).
41. Hutchinson, J. W. & Suo, Z. In *Advances in applied mechanics* Vol. 29 63–191 (Elsevier), (1991).
42. Sundaram, B. M. & Tippur, H. V. Dynamics of crack penetration vs. branching at a weak interface: an experimental study. *J. Mech. Phys. Solids* **96**, 312–332 (2016).
43. Park, B. et al. Dramatically enhanced mechanosensitivity and signal-to-noise ratio of nanoscale crack-based sensors: effect of crack depth. *Adv. Mater.* **28**, 8130–8137 (2016).
44. Cook, J. & Gordon, J. A mechanism for the control of crack propagation in all-brittle systems. *Proc. Math. Phys. Eng. Sci.* **282**, 508–520 (1964).
45. He, M.-Y. & Hutchison, J. W. Kinking of a crack out of an interface. *J. Appl. Mech.* **56**, 270–278 (1989).
46. Ming-Yuan, H. & Hutchinson, J. W. Crack deflection at an interface between dissimilar elastic materials. *Int. J. Solids Struct.* **25**, 1053–1067 (1989).
47. An, L., Pan, Y., Shen, X., Lu, H. & Yang, Y. Rod-like attapulgite/polyimide nanocomposites with simultaneously improved strength, toughness, thermal stability and related mechanisms. *J. Mater. Chem.* **18**, 4928–4941 (2008).
48. Jia, X. et al. Dramatic enhancements in toughness of polyimide nanocomposite via long-CNT-induced long-range creep. *J. Mater. Chem.* **22**, 7050–7056 (2012).
49. Ostapiuk, M., Bieniaś, J. & Surowska, B. Analysis of the bending and failure of fiber metal laminates based on glass and carbon fibers. *Sci. Eng. Compos. Mater.* **25**, 1095–1106 (2018).
50. Kim, T. et al. Polyimide encapsulation of spider-inspired crack-based sensors for durability improvement. *Appl. Sci.* **8**, 367 (2018).
51. Robinson, P., Greenhalgh, E. & Pinho, S. *Failure mechanisms in polymer matrix composites: criteria, testing and industrial applications*. (Elsevier), (2012).
52. Li, Y. et al. One-step synthesis of ultra-long silver nanowires of over 100 μm and their application in flexible transparent conductive films. *RSC Adv.* **8**, 8057–8063 (2018).
53. Mao, Y. et al. Large-scale synthesis of AgNWs with ultra-high aspect ratio above 4000 and their application in conductive thin film. *J. Mater. Sci.: Mater. Electron.* **28**, 5308–5314 (2017).
54. Wang, Y., Liu, P., Zeng, B., Liu, L. & Yang, J. Facile synthesis of ultralong and thin copper nanowires and its application to high-performance flexible transparent conductive electrodes. *Nanoscale Res. Lett.* **13**, 1–10 (2018).
55. Zhang, H. et al. High-efficiency extraction synthesis for high-purity copper nanowires and their applications in flexible transparent electrodes. *Nano Mater. Sci.* **2**, 164–171 (2020).
56. Lee, E. et al. Effect of metal thickness on the sensitivity of crack-based sensors. *Sensors* **18**, 2872 (2018).
57. Wang, B. et al. Camphor-enabled transfer and mechanical testing of centimeter-scale ultrathin films. *Adv. Mater.* **30**, 1800888 (2018).

ACKNOWLEDGEMENTS

AUTHOR CONTRIBUTIONS

T.K., I.H., M.K., S.I., J.-S.K., S.H., and D.K. led the development of the concepts, designed the experiments, interpreted results, and wrote the paper. T. Kim, I. Hong, M. Kim, and S. Im equally contributed to this work. T.K., I.H., M.K. led the experimental works and S.I. programmed machine learning algorithm, with support from Y.R., C.K., J.L., D.K., J.C. and J.P. about fabrication of ULTIMAC sensors and crack-based sensors. In addition, S.L., and D.L. provided technical guidance in measuring crack gap displacement. S.H., S.J. and C.K. have contributed to the writing of the manuscript. All authors contributed to proofreading the manuscript.

COMPETING INTERESTS

The authors declare no competing interests.

ADDITIONAL INFORMATION

Supplementary information The online version contains supplementary material available at https://doi.org/10.1038/s41528-023-00255-2.

Correspondence and requests for materials should be addressed to Je-Sung Koh, Seungyong Han or Daeshik Kang.

Reprints and permission information is available at http://www.nature.com/reprints

Publisher's note Springer Nature remains neutral with regard to jurisdictional claims in published maps and institutional affiliations.